Chemical Science

ROYAL SOCIETY OF CHEMISTRY

EDGE ARTICLE

View Article Online
View Journal | View Issue

Cite this: *Chem. Sci.*, 2025, **16**, 2785

All publication charges for this article have been paid for by the Royal Society of Chemistry

Received 17th September 2024
Accepted 2nd January 2025

DOI: 10.1039/d4sc06281g

rsc.li/chemical-science

Copper catalyzed selective methane oxidation to acetic acid using O_2†

Poorvi Gupta, Bharti Rana, Rishabh Maurya, Rahul Kalita, Manav Chauhan and Kuntal Manna *

The direct transformation of methane into C_2 oxygenates such as acetic acid selectively using molecular oxygen (O_2) is a significant challenge due to the chemical inertness of methane, the difficulty of methane C–H bond activation/C–C bond coupling and the thermodynamically favored over-oxidation. In this study, we have successfully developed a porous aluminium metal–organic framework (MOF)-supported single-site mono-copper(II) hydroxyl catalyst [MIL-53(Al)-Cu(OH)], which is efficient in directly oxidizing methane to acetic acid in water at 175 °C with a remarkable selectivity using only O_2. This heterogeneous catalyst achieved an exceptional acetic acid productivity of 11 796 $mmol_{CH_3CO_2H}$ mol_{Cu}^{-1} h^{-1} in 9.3% methane conversion with 95% selectivity in the liquid phase and can be reused at least 6 times. Our experiments, along with computational studies and spectroscopic analyses, suggest a catalytic cycle involving the formation of a methyl radical ($^{\bullet}CH_3$). The confinement of Cu-active sites within the porous MIL-53(Al) MOF facilitates C–C bond coupling, resulting in the efficient formation of acetic acid with excellent selectivity due to the internal mass transfer limitations. This work advances the development of efficient and chemoselective earth-abundant metal catalysts using MOFs for the direct transformation of methane into value-added products under mild and eco-friendly conditions.

Introduction

Acetic acid is a crucial commodity chemical in the industrial sector, with a global market volume exceeding 19 million metric tons.[1] It is used extensively as vinegar, an antiseptic, and a solvent and also serves as a precursor in the production of acetate esters, vinyl acetate monomers, and acetic anhydride.[2–4] The industrial synthesis of acetic acid involves a three-step process that is capital- and energy-intensive: (1) conversion of coal or methane into synthesis gas (syngas) through steam reforming of methane or coal gasification at high temperatures; (2) catalytic conversion of syngas to methanol at elevated temperatures; (3) subsequent rhodium or iridium catalyzed carbonylation of methanol by the Monsanto or Cativa process to yield acetic acid.[5–10] Direct conversion of methane to acetic acid utilizing only O_2 would be both environmentally friendly and economically advantageous. However, this process is extremely challenging due to methane's chemical inertness caused by its high C–H bond energy (104 kcal mol^{-1}), low polarizability, low acidity ($pK_a \sim 50$), and large HOMO–LUMO gap.[11,12] Direct oxidation of methane to acetic acid also suffers from poor productivity and selectivity due to the challenges associated with simultaneous methane C–H bond activation/C–C bond coupling and the over-oxidation of the acetic acid to produce CO and CO_2.

Several late-transition metal catalysts, such as Au/H-MOR (Au nanoparticles dispersed on mordenite),[13] Rh_1/pMOF,[14] and ZSM-5-supported-Rh,[15] Ru,[16] and Ir[17] have been developed, which utilize toxic CO along with O_2 for the conversion of methane to acetic acid. However, the use of toxic CO and precious metals, along with poor selectivity and low productivity of acetic acid, highlights the need for further advancements in designing and synthesizing catalysts for the cost-effective and environmentally sustainable production of acetic acid. Examples of catalysts enabling the conversion of methane to acetic acid using only O_2 are rare.[18–22] Recent interest has focused on metal–organic frameworks (MOFs) to develop catalysts for direct methane oxidation to valuable products.[23–36] MOFs, built from metal-oxo cluster nodes interconnected by organic linkers, have been used to develop well-defined earth-abundant metal catalysts for chemoselective reactions owing to their crystalline structure, tunable pore size, reticular synthesis, ease of post-synthetic modification and active-site isolation.[37–50] Notably, the post-synthetic metalation of MOFs' nodes allows the development of highly electrophilic base-metal catalysts, enabling methane activation *via* σ-bond metathesis.[22,27,28] In addition, the high surface area of MOFs prevents overoxidation

Department of Chemistry, Indian Institute of Technology, Hauz Khas, Delhi, New Delhi, 110016, India. E-mail: kmanna@chemistry.iitd.ac.in

† Electronic supplementary information (ESI) available: Synthesis and characterization of MIL-53(Al)-Cu(OH) catalysts, procedures and optimization of the catalytic reactions and control experiments, and details of the X-ray absorption spectroscopic analysis and DFT calculations. See DOI: https://doi.org/10.1039/d4sc06281g

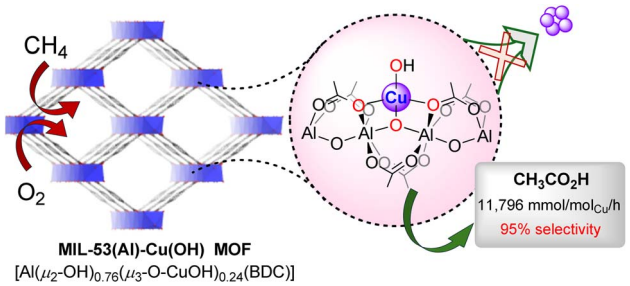

Fig. 1 Development of the porous aluminium-MOF confined mono-Cu(II) hydroxyl catalyst for the direct and selective oxidation of methane to acetic acid utilizing only O_2 as the oxidant.

by adsorbing the reactive intermediates formed during the catalysis. Moreover, the confined space within the MOF's micropores enhances the local concentration of methane around the active site and facilitates C–C coupling within the pores (Fig. 1).

We recently reported a cerium UiO-MOF's node-supported electrophilic copper(II) hydroxide catalyst, which activates methane *via* σ-bond metathesis and subsequently converts it to acetic acid using only O_2 as the oxidant.[22] We envisioned that developing MIL-53(Al) node supported Cu(II) hydroxyl species would be more efficient in activating methane in a similar manner due to the increased charge density of Al^{3+} ions and two additional oxygen atoms in the coordination sphere of the Cu^{2+} ion. Moreover, the less sterically hindered Al-oxo nodes in MIL-53(Al) would provide more accessible active copper centres compared to the UiO-MOF analogues. Herein, we report the development of a mono-copper(II) hydroxyl species confined within the porous aluminium MOF, enabling direct methane oxidation to acetic acid using O_2 at 175 °C. This process achieves a productivity of 11 796 $mmol_{CH_3CO_2H}$ mol_{Cu}^{-1} h^{-1}, with a methane conversion of 9.3% and a selectivity of 95% in the liquid phase.

Results and discussion

Synthesis and characterization of the MIL-53(Al)-Cu(OH) MOF

MIL-53(Al)-Cu(OH) was synthesized through a post-synthetic modification of the aluminium hydroxyl nodes of the MIL-53(Al) MOF, which has the chemical formula of [Al(OH)(BDC)] (H_2BDC = 1,4-benzenedicarboxylic acid). The synthesis involved a solvothermal reaction of 1,4-benzenedicarboxylic acid (H_2bdc) and $AlCl_3 \cdot 6H_2O$ in dimethylformamide (DMF) at 120 °C for 2 days, resulting in the formation of MIL-53(Al) as a white crystalline solid. In MIL-53(Al) MOF, Al^{3+} ions are coordinated in an octahedral manner with μ_2-hydroxide and 1,4-benzenedicarboxylate (bdc^{2-}) bridging linkers forming a three-dimensional porous topology with rhombic channels.[51,52] The μ_2-OH of the SBUs was deprotonated using *n*-BuLi, followed by a salt metathesis reaction of $CuCl_2$ in tetrahydrofuran (THF) to yield MIL-53(Al)-CuCl as a yellowish-green solid. Further treatment of MIL-53(Al)-CuCl with $NaEt_3BH$ in THF at room temperature facilitated halide–hydride exchange at the Cu ion, resulting in MIL-53(Al)-CuH. This material, upon subsequent treatment with water transformed into MIL-53(Al)-Cu(OH). Analysis by inductively coupled plasma optical emission spectroscopy (ICP-OES) showed that MIL-53(Al)-Cu(OH) has 24% copper loading with respect to μ_2-OH, resulting in the chemical formula of $AlO_{5.24}C_8H_5Cu_{0.24}$. The similarity in the powder X-ray diffraction (PXRD) patterns of MIL-53(Al)-CuCl, MIL-53(Al)-Cu(OH) and MIL-53(Al) reveals that the crystallinity and structure of the MIL-53(Al) MOF remained intact even after post-synthetic metalation (Fig. 2a). MIL-53(Al)-Cu(OH) has a BET surface area of 1263 m^2 g^{-1} and a pore diameter of 0.60 nm (Fig. 2b and S4, ESI†). The slightly reduced surface area of MIL-53(Al)-Cu(OH) compared to that of MIL-53(Al) (1386 m^2 g^{-1}) is ascribed to the presence of Cu(OH) species within the MOF pores (Fig. 2b). The structure and stability of the MOF were further examined by infrared spectroscopy (IR) and thermogravimetric analysis (TGA), respectively (Fig. S2 and S3, ESI†). Scanning electron microscopy (SEM) images showed that MIL-53(Al)-Cu(OH) particles are nearly spherical, with an average size of 200 nm (Fig. S5, ESI†). In the scanning electron microscopy (SEM) energy-dispersive X-ray (EDX) mapping of MIL-53(Al)-Cu(OH), it was observed that Al and Cu are uniformly distributed throughout the MOF particles (Fig. S5, ESI†).

The X-ray photoemission spectroscopy (XPS) spectrum of MIL-53(Al)-Cu(OH) showed Cu $2p_{3/2}$ binding energies at 933.13 eV and 934.37 eV with satellite peaks at 941.05 eV, 943 eV, and 944.79 eV, indicating a +2-oxidation state of the copper ion. In this XPS spectrum, the Cu $2p_{1/2}$ binding energies are centered at 952.92 eV and 954.41 eV, with satellite features at 961.52 eV, 962.96 eV and 965.49 eV, which is consistent with the presence of Cu^{2+} ions (Fig. 2c).[53] The fitted Al 2p spectrum displays four peaks at binding energies of 74.44 eV, 74.9 eV, 76.09 eV, and 78.1 eV (Fig. 2d). The peaks at 74.44 eV and 74.9 eV are assigned to the spin–orbit coupled components Al^{3+} $2p_{3/2}$ and Al^{3+} $2p_{1/2}$, respectively. Additionally, the peaks at 76.09 eV and 78.1 eV are attributed to the Cu(II) ($3p_{3/2}$–$3p_{1/2}$) doublet.[54] The existence of Cu^{2+} ions was further supported by X-ray absorption near edge structure (XANES) analysis, which demonstrated the alignment of the K-edge energy of Cu ions in MIL-53(Al)-Cu(OH) (8984.9 eV) with that of penta-coordinated Cu^{2+} (Fig. 2e).[55] The X-band electron paramagnetic resonance (EPR) spectrum of MIL-53(Al)-Cu(OH) recorded at 298 K displayed $g_{\parallel} = 2.31$, $A_{\parallel} = 159.2$ and $g_{\perp} = 2.07$ with a poorly resolved perpendicular component, corresponding to the square pyramidal geometry of Cu^{2+} ions (Fig. 2f).[56–58] Furthermore, fitting the extended X-ray absorption fine structure (EXAFS) data with the density functional theory (DFT) optimized structure of MIL-53(Al)-Cu(OH)(OH_2) (Fig. 2g) revealed that the Cu^{2+} ion has a distorted square pyramidal geometry, coordinating with one μ_3–O^- (Cu–$O^-_{\mu_3\text{–}O}$: 1.91 Å), one hydroxide (Cu–O_{OH}: 1.88 Å), two neutral carboxylate oxygen atoms (Cu–$O_{carboxylate}$: 1.95 Å) and one water molecule (Cu–O_{H_2O}: 2.42 Å) (Fig. 2i). The phase uncorrected k^2-weighted Cu-EXAFS $\chi(R)$ spectrum of MIL-53(Al)-Cu(OH) lacked the Cu···Cu scattering feature at 2.14 Å of Cu foil, further confirming the absence of Cu nanoparticles in the MIL-53(Al)-Cu(OH) MOF (Fig. 2h). The distinctive scattering

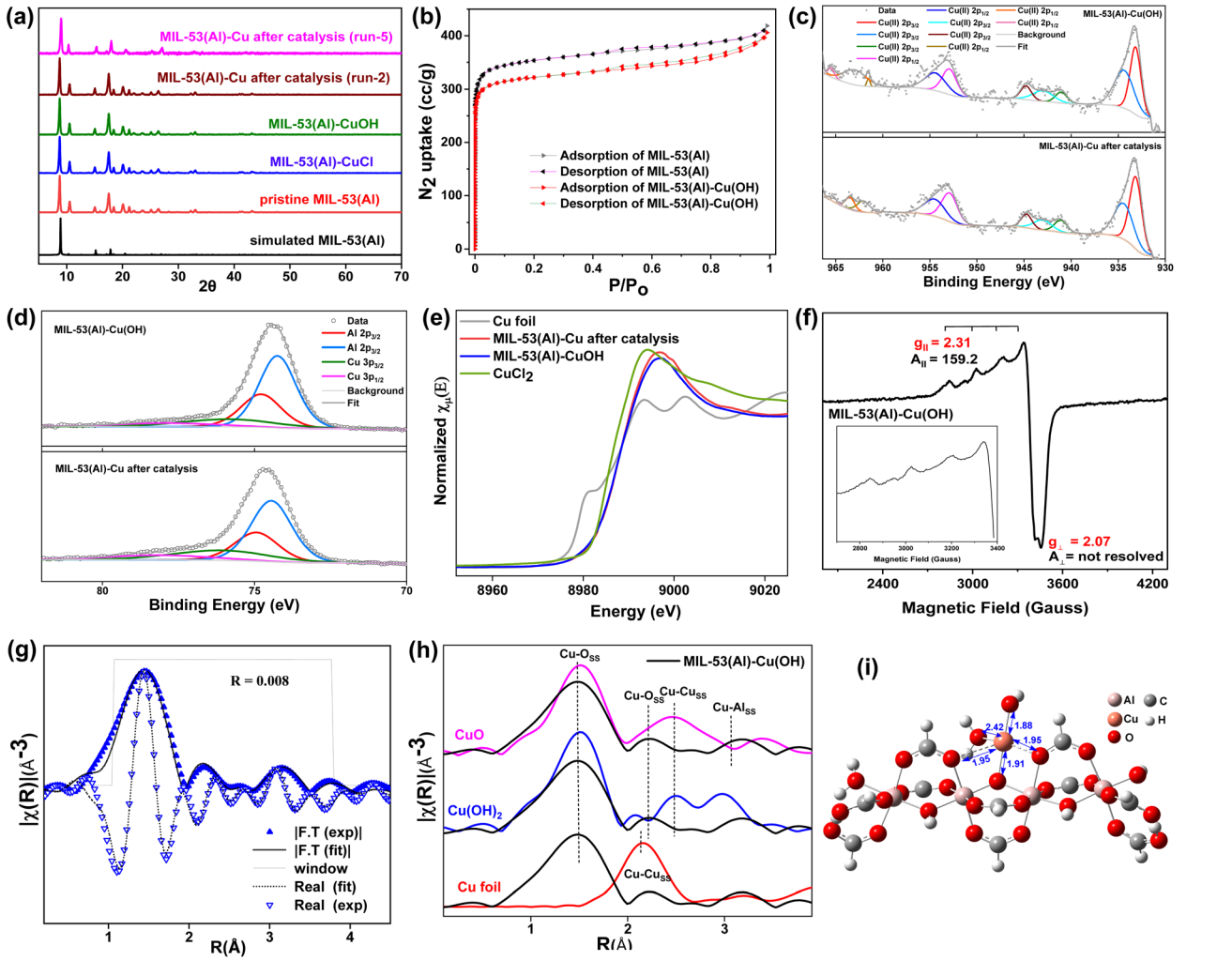

Fig. 2 (a) PXRD patterns of the simulated MIL-53(Al) MOF (black), pristine MIL-53(Al) MOF (red), MIL-53(Al)-CuCl MOF (blue), MIL-53(Al)-CuOH MOF (green), MIL-53(Al)-Cu after run-2 (wine) and run-5 of catalysis (magenta). (b) N_2 sorption isotherms of MIL-53(Al) (black) and MIL-53(Al)-Cu(OH) (red) measured at 77 K. (c) Cu 2p XPS spectra of MIL-53(Al)-Cu(OH) (top) and MIL-53(Al)-Cu after catalysis (bottom). (d) Al 2p XPS spectra of MIL-53(Al)-Cu(OH) (top) and MIL-53(Al)-Cu after catalysis (bottom). (e) Cu K-edge XANES spectra of Cu-foil (grey), $CuCl_2$ (green), MIL-53(Al)-Cu(OH) (blue) and MIL-53(Al)-Cu after catalysis (red). (f) X-band EPR spectra of MIL-53(Al)-Cu(OH) at 298 K. (g) EXAFS spectra and fits in *R*-space at the Cu K-edge of MIL-53(Al)-Cu(OH) with the magnitude and real component of the Fourier transformation shown as solid and hollow triangles in blue color, respectively. The fitting range in *R*-space is 1.1–3.8 Å (within the grey line); (h) k^2-weighted Cu-EXAFS $\chi(R)$ spectra of MIL-53(Al)-Cu(OH) (black), CuO (pink), $Cu(OH)_2$ (blue), and Cu foil (red). (i) DFT optimized structure of MIL-53(Al)-Cu(OH)(OH_2).

feature at 1.47 Å in the same spectrum corresponds to Cu–O scattering, similar to that observed in CuO and $Cu(OH)_2$ (Fig. 2h). In addition, the EXAFS data of MIL-53(Al)-Cu(OH) were also fitted to its DFT model with 5–80% metallic Cu or 5–80% CuO (Fig. S14, ESI†).

Significant discrepancies and elevated *R*-factors indicated that no metallic Cu nanoparticles or CuO were present in MIL-53(Al)-Cu(OH). The EXAFS analysis revealed that MIL-53(Al)-Cu(OH) contains node-supported single-site monomeric $Cu^{II}(OH)$ species, which have no Cu neighbours.

Catalytic performance for methane oxidation to acetic acid

MIL-53(Al)-Cu(OH) was tested as a heterogeneous catalyst for methane conversion to acetic acid using O_2 as the oxidant. The methane oxidation reactions were performed in a high-pressure batch reactor by varying the temperature, ratio of methane to O_2 in the feed, solvents, and reaction time.

The liquid products were analyzed using a gas-chromatograph equipped with a mass spectrometry (MS) detector and a flame-ionization detector (GC-FID), while the gas analysis was performed using a GC-thermal conductivity detector (GC-TCD). The quantification of liquid oxygenates was further confirmed using a high performance liquid chromatograph (HPLC) equipped with a refractive index detector. The reaction of methane (30 bar) and O_2 (10 bar) in an aqueous suspension of MIL-53(Al)-Cu(OH) (3.8 mg, 4.0 μmol Cu) at 150 °C in 32 h produced 1.15 mmol of CH_3CO_2H as the primary product along with minor quantities (9.5%) of methanol and ethanol in the liquid phase. In this reaction, no formic acid or any other oxygenated products were observed. Additionally, 0.032 mmol

of CO_2 were detected as a side product in the gas phase. The reaction conditions were further optimized to get the highest yield and selectivity of acetic acid.

Effect of solvent. Various polar and non-polar solvents were tested to optimize the yield of acetic acid for MIL-53(Al)-Cu(OH) catalyzed methane oxidation. Acetic acid was only formed in water and the catalyst was inactive in other solvents such as heptane, toluene, and THF (entries 22–24, Table S2, ESI†). This result may be attributed to the role of water as one of the reactants in the synthesis of acetic acid. Subsequently, we conducted experiments to optimize the amount of water solvent for maximizing the yield of acetic acid. 1.15 mmol of acetic acid was achieved using 7 mL of water under the same reaction conditions (150 °C, 30 bar CH_4, 10 bar O_2, and 32 h).

Effect of reaction temperature. To determine the minimum temperature required to achieve maximum acetic acid yield in methane oxidation using O_2, the influence of temperature was examined within the range of 100–200 °C with methane (30 bar) and O_2 (10 bar) over 32 h (Fig. 3a). The yields of liquid products increased as the temperature was raised from 100 to 175 °C reaching a peak of 1.51 mmol of acetic acid at 175 °C. However, when the temperature was further increased beyond 175 °C, the yield of acetic acid decreased significantly, with CO_2 as the major product. This decline in the yield of acetic acid beyond 175 °C is primarily attributed to the over-oxidation of methane (Fig. 3a).

Effect of partial pressure of O_2 and methane. To optimize the partial pressures of O_2 and methane, the total reaction vessel pressure was maintained at a constant 40 bar, balanced with nitrogen, to ensure accurate comparisons as different pressures can influence methane solubility. The effect of O_2 partial pressure on methane oxidation was investigated at 175 °C under a mixture of CH_4 (30 bar) and varying partial pressures of O_2 (2–10 bar) for 32 h. As illustrated in Fig. 3b, the optimal productivity of CH_3CO_2H (acetic acid) with MIL-53(Al)-Cu(OH) was achieved at a P_{O_2} of 10 bar. The oxidation of methane to acetic acid increased with higher partial pressures of O_2, peaking at 10 bar of O_2 pressure (entries 8–11, Table S2, ESI†). At an elevated O_2 pressure of 15 bar (entry 24, Table S3, ESI†), acetic acid selectivity dropped to 38.3%, with CO_2 becoming the major product. This suggests that higher O_2 pressures favor C–O bond formation due to the increased reactivity of carbon-centered radicals with molecular oxygen. Additionally, the methane oxidation reactions were conducted at 175 °C for 32 h in

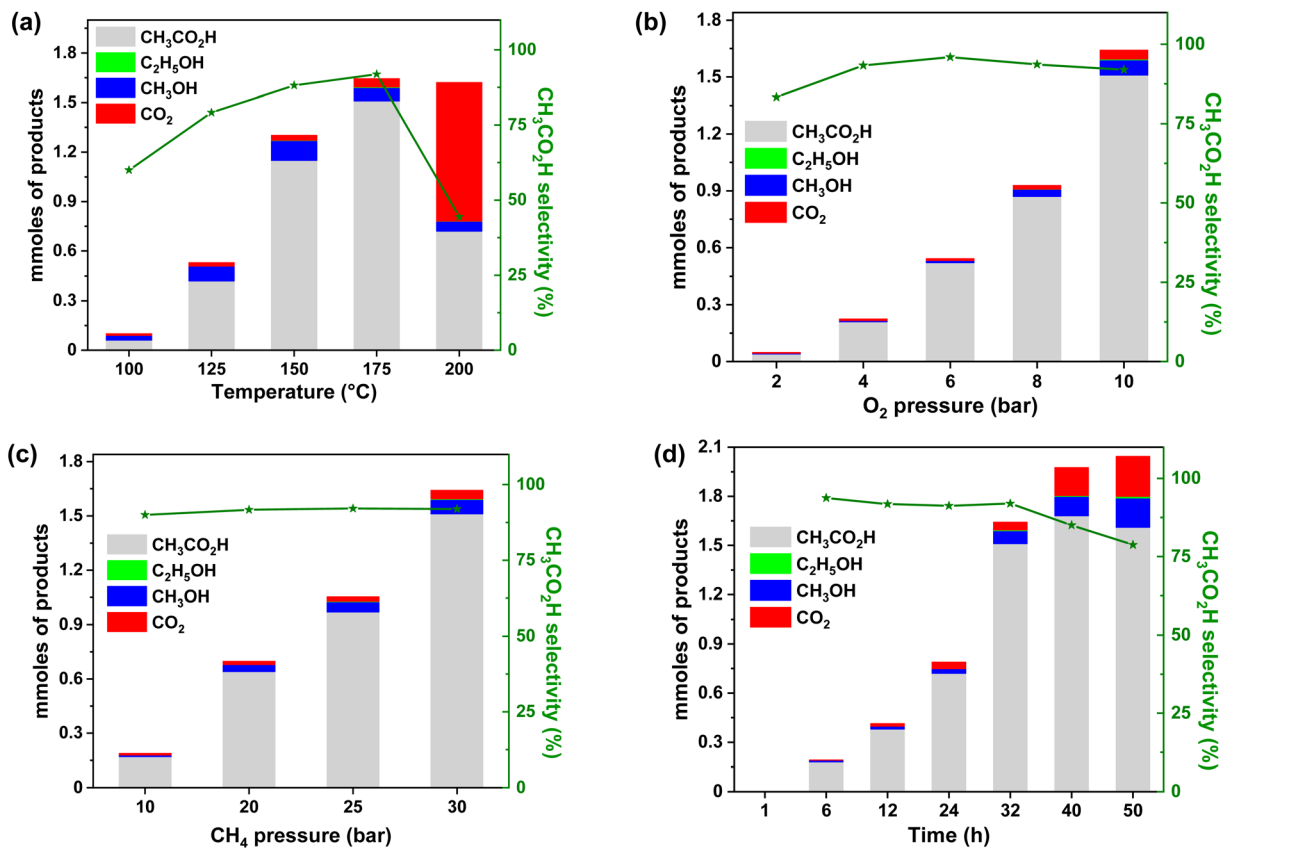

Fig. 3 (a) Effect of temperature on oxygenated product yields and selectivity of acetic acid. Reaction conditions: MIL-53(Al)-Cu(OH) (3.8 mg, 4.0 μmol), 30 bar CH_4, 10 bar O_2, 7 mL water and 32 h. (b) Effect of O_2 pressure on the oxygenated product yields and selectivity of acetic acid. Reaction conditions: MIL-53(Al)-Cu(OH) (3.8 mg, 4.0 μmol), 30 bar CH_4, 175 °C, 7 mL water and 32 h, balanced with N_2 to maintain a total pressure of 40 bar. (c) Effect of CH_4 pressure on the oxygenated product yields and selectivity of acetic acid. Reaction conditions: MIL-53(Al)-Cu(OH) (3.8 mg, 4.0 μmol), 10 bar O_2, 175 °C, 7 mL water and 32 h, balanced with N_2 to maintain a total pressure of 40 bar. (d) Effect of time on the oxygenated product yields and selectivity of acetic acid. Conditions: MIL-53(Al)-Cu(OH) (3.8 mg, 4.0 μmol), 30 bar CH_4, 10 bar O_2, 7 mL water and 175 °C.

a mixture of 10 bar of O_2 and variable methane pressures to examine the correlation between the pressure of methane and the yield of acetic acid (Fig. 3c). It was observed that the yield of acetic acid increased from 0.17 to 0.97 mmol as the methane pressure was raised from 10 to 25 bar (entries 12–14, Table S2, ESI†). The highest yield of 1.51 mmol of acetic acid was achieved at a methane pressure of 30 bar (Fig. 3c).

Effect of reaction time. The impact of reaction time on methane oxidation was evaluated over a period of 1–50 h using CH_4 (30 bar) and O_2 (10 bar) at 175 °C (Fig. 3d). The findings indicated a direct relationship between the acetic acid yield and reaction time within the 1–40 h range. Initially, no acetic acid was detected within the first hour, but as the reaction time increased, 0.18, 0.38, and 0.72 mmol of acetic acid were obtained in 6, 12 and 24 h, respectively. The highest yield of 1.51 mmol of acetic acid was achieved at 32 h, with an impressive 92% selectivity. Extending the reaction time to 40 h resulted in a slight increase in acetic acid yield to 1.68 mmol, although with reduced selectivity (84%). Further continuing the reaction to 50 h resulted in a decrease in acetic acid yield to 1.61 mmol, along with an increase in CO_2, which are thermodynamically more favorable. This decline in product selectivity can be attributed to the over-oxidation of liquid products due to the prolonged reaction time. As a result, MIL-53(Al)-Cu(OH) (3.8 mg, 4.0 μmol Cu) exhibited an exceptionally high acetic acid productivity of 377 472 $mmol_{CH_3CO_2H}$ mol_{Cu}^{-1} under 30 bar of methane and 10 bar of O_2 in 7 mL water at 175 °C for 32 h (entry 1, Table S4†) achieving ~95% liquid selectivity and ~92% overall carbon selectivity with a methane conversion of 9.3%. In the reaction, 3.2 mmol of methane is oxidized by O_2 to yield 1.51 mmol of acetic acid, 0.048 mmol of CO_2 and 1.4 mmol of H_2 (Table S5, ESI†). The total amount of carbon-containing products obtained was 3.16 mmol, based on the consumption of 3.2 mmol of methane, leading to a carbon balance of 98.75% (Table S5, ESI†).

MIL-53(Al)-Cu(OH) is recyclable for at least six consecutive cycles with consistent activity, giving a cumulative TON of 2204 (Fig. 4b). The percentages of leached Cu and Al after run-1 were 0.06 and 0.05, respectively, and after run-5 they were 0.05 and 0.08, respectively (Table S6, ESI†). The robustness of the MOF was confirmed by PXRD, XPS, and X-ray absorption studies (XAS) and ICP-analysis of the used catalyst for selective methane oxidation to acetic acid. MIL-53(Al)-Cu(OH) with a maximum productivity of 420 000 $mmol_{CH_3CO_2H}mol_{Cu}^{-1}$ exceeds the performance of all previously reported catalysts composed solely of abundant metals for methane oxidation to CH_3CO_2H (Table S13, ESI†).

Control experiments

Several controlled experiments were conducted to identify the actual catalytic species responsible for MIL-53(Al)-Cu(OH) catalyzed oxidation of methane to acetic acid. No acetic acid was detected when the reaction was conducted without a catalyst or without O_2 (entries 2 and 3, Table S2†). In addition, the catalytic reaction under N_2 instead of CH_4 did not produce any carbon-containing products, confirming CH_4 as the exclusive carbon source for acetic acid formation (entry 11, Table S3†). The production of CH_3CO_2H at 175 °C *via* CH_4 oxidation using O_2 was further confirmed using isotopically labeled $^{13}CH_4$. The reaction catalyzed by MIL-53(Al)-Cu(OH) generated $^{13}CH_3{}^{13}CO_2H$, as verified by carbon-13 nuclear magnetic resonance (^{13}C NMR) spectroscopy and gas chromatography-mass spectrometry (GC-MS) (Fig. S19†). It is noteworthy that the methane oxidation reaction ceased upon removal of the solid MIL-53(Al)-Cu(OH) MOF from the reaction mixture, confirming the embedding of the active catalytic species within the MOF (Fig. S6, ESI†). Importantly, $Cu(OH)_2$ and CuO proved to be inactive for methane oxidation under identical reaction conditions (entries 8 and 14, Table S3† or Fig. 5). Similarly, the pristine MIL-53(Al) MOF, MIL-53(Al)-CuCl, MIL-53(Al) encapsulated Cu(0) nanoparticles [Cu@MIL-53(Al)], or alumina-supported Cu(II) also failed to yield acetic acid under identical reaction conditions and Cu-loading, underscoring that Cu(OH) confined within the MIL-53(Al) MOF pores is the genuine catalytic species for methane oxidation (entries 2, 4, 15, and 7,

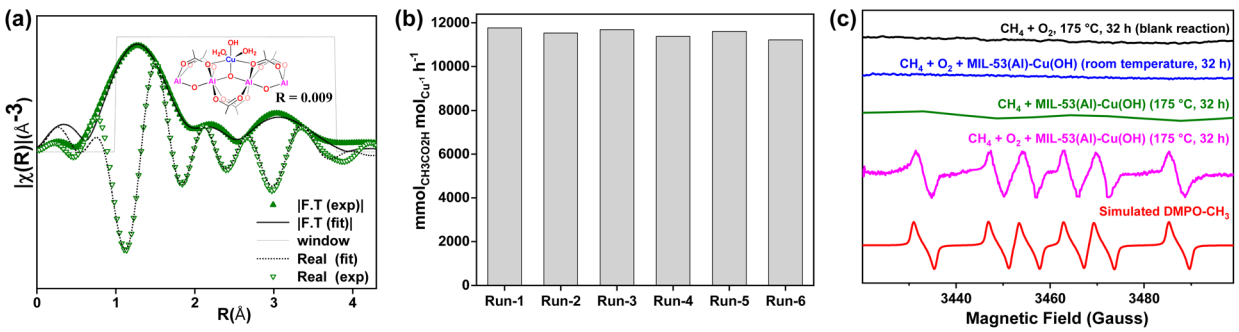

Fig. 4 (a) EXAFS spectra and fits in *R*-space at the Cu K-edge of MIL-53(Al)-Cu after catalysis with the magnitude and real component of the Fourier transformation shown as solid and hollow triangles in green color, respectively. The fitting range in *R*-space is 1.1–3.8 Å (within the grey line). (b) Plot of productivity of acetic acid in various runs during recycling and reuse of the MIL-53(Al)-Cu(OH) catalyst for the methane oxidation reaction. (c) X-band (9.85 GHz) EPR spectroscopic spin-trapping experiments. EPR spectrum from the DMPO spin-trapping experiment of uncatalyzed methane oxidation by O_2 at 175 °C (black), MIL-53(Al)-Cu(OH)-catalyzed oxidation of methane by O_2 at room temperature (blue), MIL-53(Al)-Cu(OH) catalyzed methane oxidation in the absence of O_2 at 175 °C (green), MIL-53(Al)-Cu(OH) catalyzed oxidation of CH_4 (30 bar) by O_2 (10 bar) at 175 °C for 32 h (magenta), and simulated DMPO-CH_3 (red).

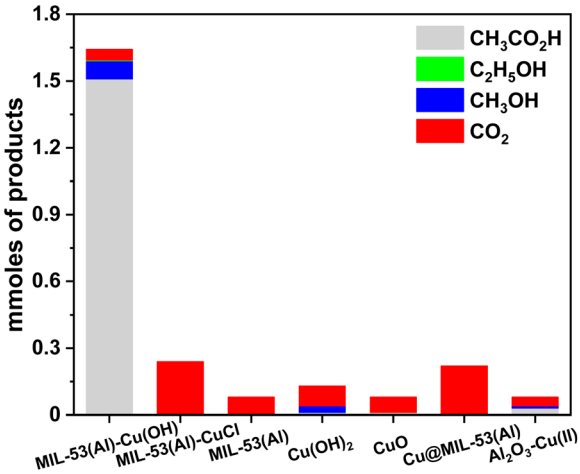

Fig. 5 Comparison of the catalytic efficiency of MIL-53(Al)-Cu(OH) with other materials in direct methane oxidation to acetic acid under identical reaction conditions. Conditions: 30 bar CH_4, 10 bar O_2, 175 °C and 32 h.

Table S3† or Fig. 5). Moreover, the PXRD patterns of the MOF recovered after catalysis showed no characteristic peak of Cu nanoparticles at higher 2θ angles (Fig. 2a).

To investigate the impact of pore sizes of the MIL-53(Al) MOF on acetic acid selectivity, we synthesized isoreticular DUT-5(Al)-Cu(OH), which has a larger pore size (0.78 nm) than MIL-53(Al)-Cu(OH) (0.6 nm). Under identical reaction conditions and equivalent Cu loading, DUT-5(Al)-Cu(OH) exhibited lower acetic acid selectivity, producing only 0.08 mmol of acetic acid, 0.04 mmol of methanol, and a higher amount of CO_2 (0.9 mmol). These experiments suggest that the increased selectivity for acetic acid associated with smaller pore sizes of MIL-53(Al)-Cu(OH) is likely due to internal mass transfer limitation of the product. The larger channels of DUT-5(Al) allow acetic acid molecules to diffuse more easily, which can lead to their over-oxidation. In contrast, the smaller pore size of MIL-53(Al)-Cu(OH) restricts the diffusion of larger acetic acid molecules (5.9 Å), allowing only smaller molecules like methane (3.8 Å) to access the catalytic copper sites within the pores. This internal mass transfer limitation effectively enhances the production of acetic acid with excellent selectivity by preventing its over-oxidation within the pores of MIL-53(Al)-Cu(OH). Thus, under identical conditions with equivalent copper loading, MIL-53(Al)-Cu(OH) demonstrates greater reactivity and selectivity for acetic acid production compared to MIL-53(Al)-CuCl, $Cu(OH)_2$, CuO, Al_2O_3-supported Cu(II), and DUT-5(Al)-Cu(OH). This emphasizes the critical role of the MOF's node-supported single-site mono-Cu^{II}(OH) species confined within the uniform pores in chemoselective oxidation of methane.

Mechanistic exploration of MIL-53(Al)-Cu(OH) catalyzed oxidation of methane to acetic acid

To investigate the mechanism for MIL-53(Al)-Cu(OH)-catalyzed oxidation of methane to acetic acid, the oxidation state and coordination environment of the MOF recovered after catalysis were analyzed. The XPS of recovered MIL-53(Al)-Cu confirmed the +2 oxidation state of Cu ions in the MOF after catalysis (Fig. 2c). The K-edge energy of 8985.6 eV for the recovered MOF also showed that Cu is in a +2 oxidation state, with an octahedral geometry (Fig. 2e).[59] The prediction of the geometries can be further established by the white line intensity. The K edge energy is attributed to the transition from 1s – $4p_{xy}$, while the transition from 1s – $4p_x$ is associated with white line intensity. The increase in axial coordination led to an increase in the white line intensity of the recovered MOF. The EXAFS data of the MOF recovered after catalysis fitted well with the DFT-optimized model of MIL-53(Al)-Cu(OH)$(OH_2)_2$, which suggests that Cu in the MOF recovered after catalysis adopted a distorted octahedral geometry (Fig. S13, ESI†).

Additionally, fitting the EXAFS spectra with the DFT model of MIL-53(Al)-Cu(OH) containing 5–80% CuO or 5–80% metallic Cu showed significant deviations and elevated *R* factors, indicating the absence of any Cu nanoparticles or CuO within the MOF post catalysis (Fig. S15, ESI†). These findings demonstrate that Cu nanoparticles or CuO does not serve as the active catalytic species in the oxidation of methane. Instead, they highlight the pivotal role of single-site Cu(OH) species supported on the MOF nodes in driving the chemoselective oxidation of methane.

Radical trap experiments were conducted to explore the involvement of $^{\bullet}OH$ or $^{\bullet}CH_3$ radicals in MIL-53(Al)-Cu(OH) catalyzed oxidation of methane using O_2. The rate of acetic acid production remained unchanged in the presence of $^{\bullet}OH$ scavengers such as Na_2SO_3 or *tert*-butanol (entries 5 and 20, Table S3†), eliminating the role of $^{\bullet}OH$ in the conversion of methane to acetic acid using O_2. However, radical trapping experiments conducted with a $^{\bullet}CH_3$ scavenger, such as TEMPO (2,2,6,6-tetramethylpiperidine 1-oxyl), showed a reduction in acetic acid formation to 0.34 mmol (entry 22, Table S3†) under identical reaction conditions, which indicates the involvement of $^{\bullet}CH_3$ radicals in the reaction mechanism. The potential free radicals generated during the reaction were captured using the spin-trapping agent 5,5-dimethyl-1-pyrroline *N*-oxide (DMPO). The EPR spectrum of MIL-53(Al)-Cu(OH)-catalyzed methane oxidation in the presence of O_2 and DMPO at ambient temperature did not show any $^{\bullet}CH_3$ radicals (Fig. 4c). However, the supernatant after catalysis by MIL-53(Al)-Cu(OH) at 175 °C with DMPO revealed a six-line signal characteristic of the DMPO-CH_3 radical adduct, closely matching the simulated model (Fig. 4c and Table S12, ESI†). In both cases, there were no $^{\bullet}OH$ and $H_2O^{\bullet}$ radicals detected, aligning with the observation that acetic acid formation cannot be suppressed by $^{\bullet}OH$ scavengers such as Na_2SO_3 or *t*-butanol. These experiments suggest that the $^{\bullet}CH_3$ is involved in the CH_4 oxidation to acetic acid. No radical adduct was observed in the absence of MIL-53(Al)-Cu(OH) (Fig. 4c), indicating that CH_4 activation requires Cu-active sites. Importantly, no $^{\bullet}CH_3$ signal was observed when the reaction was performed in the absence of O_2 at 175 °C, suggesting that the methyl radical is only generated by the CH_4-loaded MIL-53(Al)-Cu(OH) MOF in the presence of O_2 at 175 °C.

Based on the above spectroscopic and experimental observations, we propose that MIL-53(Al)-Cu(OH) initially reacts with

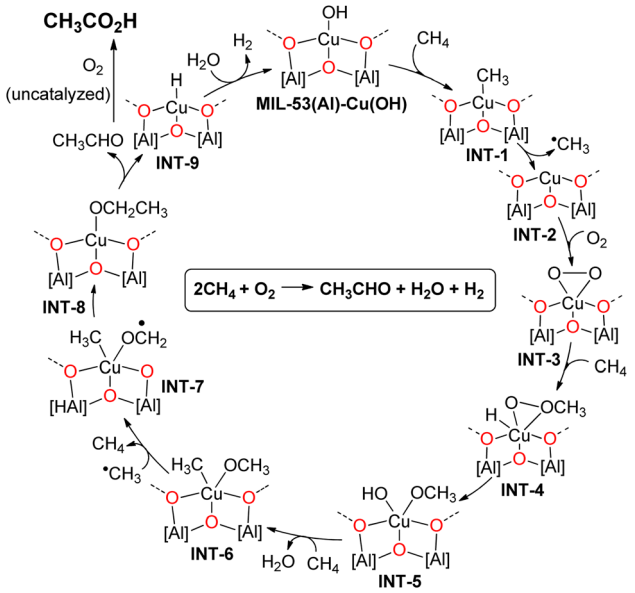

Fig. 6 The proposed catalytic cycle for MIL-53(Al)-Cu(OH) catalyzed direct oxidation of methane to acetic acid using O_2.

CH_4 to form MIL-53(Al)-$Cu^{II}(CH_3)$ (INT-1) and H_2O *via* σ-bond metathesis between Cu–OH and C–H bonds (Fig. 6). Since the direct insertion of triplet O_2 into the Cu–CH_3 bond of INT-1 is spin-forbidden,[60,61] we propose that INT-1 undergoes homolytic cleavage at 175 °C, forming a Cu(I) species (INT-2) and a $^{\bullet}CH_3$ radical. INT-2 then reacts with O_2 to form a Cu-OO$^{\bullet}$ species, which undergoes spin crossover to generate Cu(III)-η^2-peroxy species (INT-3).[62,63] In the next step, INT-3 participates in σ-bond metathesis with CH_4, resulting in the formation of INT-4. INT-4 rearranges to form INT-5, which undergoes σ-bond metathesis with CH_4, producing INT-6. Subsequently, a previously generated $^{\bullet}CH_3$ radical abstracts a hydrogen from the methoxy group of INT-6, yielding INT-7 and CH_4. INT-7 then rearranges to form INT-8, which undergoes β-hydride elimination, producing acetaldehyde and MIL-53(Al)-Cu-H (INT-9). Hydrolysis of INT-9 regenerates MIL-53(Al)-Cu(OH), thus completing the catalytic cycle (Fig. 6).

The acetaldehyde is subsequently oxidized by O_2 to form acetic acid. In order to confirm the role of MIL-53(Al)-Cu(OH) in the transformation of acetaldehyde to acetic acid, we conducted an experiment where we oxidized acetaldehyde under 10 bar of O_2 and 30 bar of N_2 at 175 °C in the presence or absence of the MOF catalyst. The results of these reactions revealed that the rate of oxidation of acetaldehyde to acetic acid remained unchanged in both cases, ruling out the involvement of MIL-53(Al)-Cu(OH) in the oxidation of acetaldehyde (entries 18 and 19, Table S3, ESI†). In addition, a small quantity of acetaldehyde was detected in the GC-FID spectrum, when the reaction was conducted for a shorter duration (18 h), which suggests that acetaldehyde might be a potential reaction intermediate in the methane to acetic acid conversion. Furthermore, the formation of a stoichiometric amount of H_2 with respect to acetic acid further supports the balanced chemical equation depicted in Fig. 6. According to this equation, the MIL-53(Al)-Cu(OH) catalyzed reaction between methane and O_2 first produces acetaldehyde, water and H_2. Then, the *in situ* generated acetaldehyde is oxidized by O_2 to furnish acetic acid.

We then attempted to synthesize potential intermediates to further support our proposed catalytic cycle. We synthesised MIL-53(Al)-Cu(OC_2H_5) (INT-8), by treating MIL-53(Al)-CuH with ethanol and tested its catalytic activity. Notably, MIL-53(Al)-Cu(OH) and MIL-53(Al)-Cu(OC_2H_5) show similar catalytic activities in the oxidation of methane to acetic acid under identical reaction conditions, indicating MIL-53(Al)-Cu(OC_2H_5) as a potential intermediate and supporting our proposed catalytic cycle (entry 21, Table S3†). Furthermore, the reaction of ethanol and O_2 also yields 0.35 mmol CH_3CO_2H under identical reaction conditions in the presence of MIL-53(Al)-Cu(OH) (entry 12, Table S3†), suggesting that the small amount of ethanol generated during the reaction is oxidized to acetic acid.

Several controlled experiments were carried out to assess the involvement of *in situ* generated CO, CO_2, and methanol as potential intermediates in the formation of CH_3CO_2H. The reaction between CH_4 and CO or CH_4 and CO_2 did not result in the formation of CH_3CO_2H (entries 9 and 13, Table S3†), ruling out acetic acid production *via* methane carbonylation or the reaction of methane with CO_2. Additionally, the reaction between methanol and CO also failed to produce any significant amount of CH_3CO_2H (entry 17, Table S3†), excluding the possibility of acetic acid formation through methanol carbonylation.

Based on the above observations, we proposed that CH_4 is oxidised to CH_3CO_2H in the presence of O_2 *via* the $^{\bullet}CH_3$ radical pathway with ethanol and acetaldehyde as the key intermediates. To further explore the reaction mechanism and identify the turnover-limiting step (TLS), the complete catalytic cycle was examined through DFT calculations (Fig. 7). The DFT-calculated energy profile diagram indicates that methane C–H bond activation through σ-bond metathesis has an energy barrier of 35 kcal mol^{-1}, while the formation of INT-1 from MIL-53(Al)-Cu(OH) is endergonic by 13.3 kcal mol^{-1}. The subsequent homolytic cleavage of INT-1 to form INT-2 (Cu^+ species) and a methyl radical is endergonic by 8.1 kcal mol^{-1}. INT-2 reacts with O_2 to form a Cu-OO$^{\bullet}$ species, which is exergonic by 35.6 kcal mol^{-1}, and this process is followed by a spin crossover to form INT-3 (Cu(III)-η^2-peroxy species), with a barrier of 6.8 kcal mol^{-1}. INT-3 undergoes σ-bond metathesis with CH_4 through TS-2, leading to the formation of INT-4 with an energy barrier of 27.1 kcal mol^{-1}. INT-4 rearranges to form INT-5, which is exergonic by 4.2 kcal mol^{-1}, and INT-5 undergoes another σ-bond metathesis *via* TS-3 to generate INT-6 with a barrier of 26.4 kcal mol^{-1}. The $^{\bullet}CH_3$ abstracts a hydrogen atom from the methoxy group of INT-6, generating INT-7, which is exergonic by 63.7 kcal mol^{-1}. INT-7 then rearranges to form INT-8, which is exergonic by 9 kcal mol^{-1}. Finally, INT-8 undergoes beta hydride elimination *via* TS-4, which is exergonic by 17.9 kcal mol^{-1} to yield acetaldehyde and MIL-53(Al)-CuH species (INT-9). MIL-53(Al)-CuH is then hydrolysed to regenerate the catalyst MIL-53(Al)-Cu(OH), which is an exergonic process by 3 kcal mol^{-1}. The energy profile diagram reveals that methane C–H bond activation through σ-bond

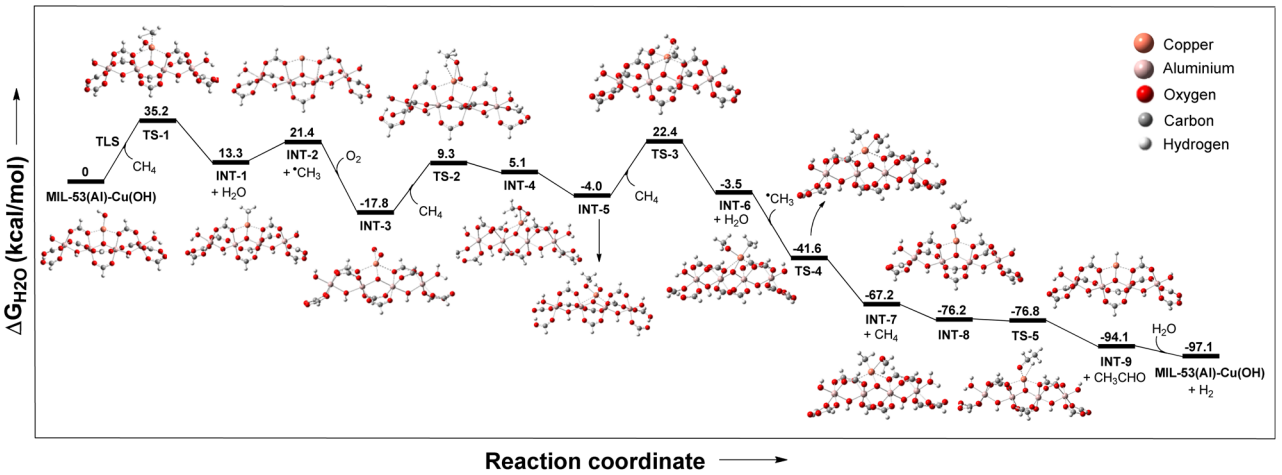

Fig. 7 DFT calculated free energy diagram at 448 K for MIL-53(Al)-Cu(OH) catalyzed methane to acetaldehyde conversion.

metathesis presents the highest energy barrier in the catalytic cycle, identifying it as the turnover-limiting step. As mentioned earlier, no methyl radical was detected in the EPR spectrum of a DMPO-loaded reaction mixture of methane (30 bar) and the MIL-53(Al)-Cu(OH) catalyst in the absence of O_2, despite the fact that $^{\bullet}CH_3$ is likely formed prior to the addition of O_2 as shown in the catalytic cycle. The DFT calculated energy profile diagram showed that the conversion of INT-1 to INT-2 is thermodynamically uphill by 8.1 kcal mol^{-1}. Therefore, the concentration of $^{\bullet}CH_3$ remains very low in the absence of O_2. However, during the methane oxidation in the presence of O_2, INT-2 rapidly reacts with O_2 to form INT-3, which is highly exergonic (downhill by 39.2 kcal mol^{-1}). This mechanistic insight, supported by DFT and experimental evidence, underscores the critical role of O_2 in driving the reaction forward and aligns with the observed catalytic behavior of the system.

Conclusions

In conclusion, we have developed a highly active single-site and heterogeneous earth-abundant metal catalyst for direct methane oxidation to acetic acid using only O_2. The catalyst displayed an outstanding productivity of 377 472 $mmol_{CH_3CO_2H}$ mol_{Cu}^{-1} and maintained 95% liquid selectivity over six consecutive runs without any loss in activity. The catalytic pathway of the MIL-53(Al)-Cu(OH) catalyst differs from that of our previously reported cerium-UiO MOF node-supported copper(II)-hydroxyl catalysts, [Ce-UiO-66-Cu(OH)].[22] In the case of the Ce-UiO-66-Cu(OH) catalyst, the conversion of methane to acetic acid occurs at 115 °C through a non-radical pathway, where the carbonylation of methane with CO forms acetic acid. This difference in mechanism can be attributed to the distinct reaction temperatures. For the MIL-53(Al)-Cu(OH) catalyzed transformation of methane to acetic acid, the homolytic cleavage of the 'Cu–CH_3' species is likely favored at 175 °C; however, this process does not occur under the operating conditions of 115 °C used for the Ce-UiO-66-Cu(OH) catalyst. Spectroscopic analyses and controlled experiments suggested that the direct oxidation of methane to acetic acid occurs *via* a catalytic cycle, where methane is first oxidized to acetaldehyde mediated by MIL-53(Al)-Cu(OH), followed by the further thermal oxidation of acetaldehyde to acetic acid by O_2. This research provides valuable insights for the development of environmentally friendly heterogeneous catalysts using abundant metals, enabling the efficient activation and partial C–H methane oxidation to acetic acid under mild and eco-friendly reaction conditions.

Experimental section

Synthesis of MIL-53(Al)-Cu(OH)

To synthesize the MIL-53(Al) MOF, 1,4-benzenedicarboxylic acid (0.050 g, 0.301 mmol) and $AlCl_3 \cdot 6H_2O$ (0.048 g, 0.198 mmol) were dissolved in 3 mL DMF. The mixture was then transferred to a Teflon lined hydrothermal autoclave, sealed, and heated at 120 °C for 48 h. After cooling to room temperature, the resultant white solid of the MIL-53(Al) MOF was collected and washed several times with DMF, followed by THF. Inside a glovebox, 50 μL of *n*-BuLi (1.65 M in cyclohexane) was added to a slurry of MIL-53(Al) (0.015 g) in 1 mL of THF and the mixture was slowly stirred at room temperature for 1.5 h. The solid was washed with THF several times and then treated with a THF solution of $CuCl_2$ (0.042 g, 0.312 mmol). The mixture was stirred overnight at room temperature. The resultant green solid of MIL-53(Al)-CuCl was isolated by centrifugation and washed with THF. Then, 40 μL of $NaEt_3BH$ (1 M in THF) was added dropwise to a slurry of MIL-53(Al)-CuCl (0.016 g) in 1 mL of THF at room temperature. After 1 h, dark violet solid MIL-53(Al)-CuH was collected by centrifugation, followed by washing several times with THF. The MOF was then immersed in water in a vial for 30 minutes to yield MIL-53(Al)-Cu(OH). ICP-OES analysis shows a 24% copper loading relative to the μ_2-OH moiety, resulting in an empirical formula of $AlO_{5.24}C_8H_5Cu_{0.24}$ for MIL-53(Al)-Cu(OH). The structure of the MOF was confirmed by PXRD and the active Cu^{II}(OH) site was characterized by XPS, EPR, and X-ray absorption spectroscopy (XAS).

MIL-53(Al)-Cu(OH) catalyzed methane oxidation

Catalytic methane oxidation was performed in a high-pressure glass-lined batch reactor (100 mL, Amar Equipment) equipped with a thermocouple. MIL-53(Al)-Cu(OH) as the catalyst was added to the glass liner containing 7 mL of water. The reactor was sealed and purged twice with CH_4. The reactor was then pressurized with CH_4 (30 bar) and O_2 (10 bar) and heated to the desired temperature. After the specified reaction time, the reactor was cooled to room temperature, and the products in both the liquid and gaseous phases were analyzed using gas chromatography.

Analysis and quantification of products

The liquid phase products from the catalytic reactions were analyzed using an Agilent 8890 GC equipped with a flame ionization detector (FID) and an Agilent 7890B GC with a mass detector (Agilent 5977B GC/MSD). The post-reaction gas was analyzed using an Agilent 8890 GC, equipped with a PoraPlot Q column, a molecular sieves column, and a thermal conductivity detector (TCD) (Section 3.2, ESI†). After 32 h, the reactor was cooled to room temperature. The gas sample was collected and analyzed using GC-TCD. Quantification of CH_4 and CO_2 was achieved by measuring the amounts of each gas in the reactor's headspace. The response factors were determined using a standard analytical gas mixture. A 1 mL aliquot of the liquid sample was transferred to a GC vial, and 5 μL of ethylene glycol (internal standard) was added. This sample was then analyzed by GC-FID/MS to identify and quantify the products in the liquid phase. A 1 μL sample was injected into the GC, and quantification was done using standard calibration curves. Additionally, the liquid phase products were confirmed using high-performance liquid chromatography (HPLC) with an Agilent 1260 Infinity II liquid chromatograph equipped with a refractive index detector (Agilent 1260 Infinity II). An Agilent Hi-Plex H column (300 mm length, 7 mm internal diameter, and 8 μm particle size) was used, with 100% Milli-Q water as the mobile phase. The chromatographic conditions included a flow rate of 0.7 mL min^{-1}, an injection volume of 100.0 μL, a column oven and a detector temperature of 35.0 °C, and a total run time of 45 minutes. The products in the case of HPLC were quantified using the calibration plot of 2-butanone as the internal standard.

Data availability

The data supporting this article have been included as part of the ESI.†

Author contributions

P. G. synthesized the MOF catalyst and performed catalytic reactions and DFT calculations. P. G., B. R., R. K. and M. C. characterized the MOF materials and analyzed the data. K. M. designed and supervised the entire project. K. M. and P. G. wrote the manuscript. All the authors approved the final version of the manuscript.

Conflicts of interest

There are no conflicts to declare.

Acknowledgements

KM thanks the Science and Engineering Research Board (SERB), India [CRG/2022/003553] and CSIR-HRDG [01(3040)/21/EMR-II] for financial support. P. G., B. R., R. K., and M. C. acknowledge CSIR; R. M. acknowledges UGC for financial support. We acknowledge the Raja Ramanna Centre for Advanced Technology-Indore (RRCAT) for XAS measurement at the Indus-2 SRS facility. Dr Biplab Ghosh is gratefully thanked for his help in XAFS measurement at RRCAT. The authors acknowledge the Department of Chemistry, IIT Delhi, for ICP-OES, TGA, FT-IR, and PXRD. The authors acknowledge the Central Research Facility, IIT Delhi, for XPS, SEM, BET and other instrumental facilities. The authors thank the IIT Delhi HPC facility for computational resources.

References

1 *Acetic acid global market*, 2015–2030, **https://www.statista.com/statistics/1245203/acetic-acid-market-volume-worldwide/**, accessed 10 April 2024.
2 F. N. Harris, *J. Pet. Technol.*, 1961, **13**, 637–639.
3 C. Le Berre, P. Serp, P. Kalck and G. P. Torrence, in *Ullmann's Encyclopedia of Industrial Chemistry*, John Wiley & Sons, Ltd, 2014, pp. 1–34.
4 A. C. Micciche, R. D. Barabote, D. K. Dittoe and S. C. Ricke, *J. Environ. Sci. Health, Part B*, 2020, **55**, 447–454.
5 A. D. Singh and N. W. Krase, *Ind. Eng. Chem.*, 1935, **27**, 909–914.
6 J. F. Knifton, *J. Catal.*, 1985, **96**, 439–453.
7 G. J. Sunley and D. J. Watson, *Catal. Today*, 2000, **58**, 293–307.
8 C. M. Thomas and G. Süss-Fink, *Coord. Chem. Rev.*, 2003, **243**, 125–142.
9 A. W. Budiman, J. S. Nam, J. H. Park, R. I. Mukti, T. S. Chang, J. W. Bae and M. J. Choi, *Catal. Surv. Asia*, 2016, **20**, 173–193.
10 R. L. Pruett, *Science*, 1981, **211**, 11–16.
11 H. Schwarz, *Angew. Chem., Int. Ed.*, 2011, **50**, 10096–10115.
12 W. Taifan and J. Baltrusaitis, *Appl. Catal., B*, 2016, **198**, 525–547.
13 W. Wang, W. Zhou, Y. Tang, W. Cao, S. R. Docherty, F. Wu, K. Cheng, Q. Zhang, C. Copéret and Y. Wang, *J. Am. Chem. Soc.*, 2023, **145**, 12928–12934.
14 H. Li, C. Xiong, M. Fei, L. Ma, H. Zhang, X. Yan, P. Tieu, Y. Yuan, Y. Zhang, J. Nyakuchena, J. Haung, X. Pan, M. M. Waegele, D. Jiang and D. Wang, *J. Am. Chem. Soc.*, 2023, **145**, 11415–11419.
15 J. Shan, M. Li, L. F. Allard, S. Lee and M. F. Stephanopoulus, *Nature*, 2017, **551**, 605–608.
16 R. Lanza, S. G. Järås and P. Canu, *Appl. Catal., A*, 2007, **325**, 57–67.

17 H. Li, M. Fei, J. L. Troiano, L. Ma, X. Yan, P. Tieu, Y. Yuan, Y. Zhang, T. Liu, X. Pan, G. W. Brudvig and D. Wang, *J. Am. Chem. Soc.*, 2023, **145**, 769–773.
18 J. Cao, R. J. Lewis, G. Qi, D. Bethell, M. J. Howard, B. Harrison, B. Yao, Q. He, D. J. Morgan, F. Ni, P. Sharma, C. J. Kiely, X. Li, F. Deng, J. Xu and G. J. Hutchings, *ACS Catal.*, 2023, **13**, 7199–7209.
19 W. Zhang, D. Xi, Y. Chen, A. Chen, Y. Jiang, H. Liu, Z. Zhou, H. Zhang, Z. Liu, R. Long and Y. Xiong, *Nat. Commun.*, 2023, **14**, 3047.
20 G. Qi, T. E. Davies, A. Nasrallah, M. A. Sainna, A. G. R. Howe, R. J. Lewis, M. Quesne, C. R. A. Catlow, D. J. Willock, Q. He, D. Bethell, M. J. Howard, B. A. Murrer, B. Harrison, C. J. Kiely, X. Zhao, F. Deng, J. Xu and G. J. Hutchings, *Nat. Catal.*, 2022, **5**, 45–54.
21 J. Wang, L. Zhang, D. Zeng, W. Wang, R. Li, T. Jia, B. Cui, H. Chu and W. Wang, *Appl. Catal., B*, 2023, **338**, 123062.
22 N. Antil, M. Chauhan, N. Akhtar, R. Kalita and K. Manna, *J. Am. Chem. Soc.*, 2023, **145**, 6156–6165.
23 Á. Szécsényi, G. Li, J. Gascon and E. A. Pidko, *Chem. Sci.*, 2018, **9**, 6765–6773.
24 W. Begum, M. Chauhan, R. Kalita, P. Gupta, N. Akhtar, N. Antil, R. Newar and K. Manna, *ACS Catal.*, 2024, **14**, 10427–10436.
25 B. Rungtaweevoranit, A. M. Abdel-Mageed, P. Khemthong, S. Eaimsumang, K. Chakarawet, T. Butburee, B. Kunkel, S. Wohlrab, K. Chainok, J. Phanthasri, S. Wannapaiboon, S. Youngjan, T. Seehamongkol, S. Impeng and K. Faungnawakij, *ACS Appl. Mater. Interfaces*, 2023, **15**, 26700–26709.
26 T. Ikuno, J. Zheng, A. Vjunov, M. Sanchez-Sanchez, M. A. Ortuño, D. R. Pahls, J. L. Fulton, D. M. Camaioni, Z. Li, D. Ray, B. L. Mehdi, N. D. Browning, O. K. Farha, J. T. Hupp, C. J. Cramer, L. Gagliardi and J. A. Lercher, *J. Am. Chem. Soc.*, 2017, **139**, 10294–10301.
27 L. S. Andrade, H. H. L. B. Lima, C. T. P. Silva, W. L. N. Amorim, J. G. R. Poço, A. López-Castillo, M. V. Kirillova, W. A. Carvalho, A. M. Kirillov and D. Mandelli, *Coord. Chem. Rev.*, 2023, **481**, 215042.
28 N. Antil, M. Chauhan, N. Akhtar, R. Newar, W. Begum, J. Malik and K. Manna, *ACS Catal.*, 2022, **12**, 11159–11168.
29 M. Wu, M. Miao, W. Li, X. Zhang, L. Zhang, T. Zhen, Y. Fu, J. Jin and L. Yuan, *Fuel*, 2023, **331**, 125575.
30 J. N. Hall and P. Bollini, *Chem.–Eur. J.*, 2020, **26**, 16639–16643.
31 M. Barona and R. Q. Snurr, *ACS Appl. Mater. Interfaces*, 2020, **12**, 28217–28231.
32 F. Tavani, A. Tofoni and P. D'Angelo, *Catalysts*, 2023, **13**, 1338.
33 J. Sui, M.-L. Gao, B. Qian, C. Liu, Y. Pan, Z. Meng, D. Yuan and H.-L. Jiang, *Sci. Bull.*, 2023, **68**, 1886–1893.
34 J. Baek, B. Rungtaweevoranit, X. Pei, M. Park, S. C. Fakra, Y.-S. Liu, R. Matheu, S. A. Alshmimri, S. Alshehri, C. A. Trickett, G. A. Somorjai and O. M. Yaghi, *J. Am. Chem. Soc.*, 2018, **140**, 18208–18216.
35 M. C. Simons, S. D. Prinslow, M. Babucci, A. S. Hoffman, J. Hong, J. G. Vitillo, S. R. Bare, B. C. Gates, C. C. Lu, L. Gagliardi and A. Bhan, *J. Am. Chem. Soc.*, 2021, **143**, 12165–12174.
36 J. Zheng, J. Ye, M. A. Ortuño, J. L. Fulton, O. Y. Gutiérrez, D. M. Camaioni, R. K. Motkuri, Z. Li, T. E. Webber, B. L. Mehdi, N. D. Browning, R. L. Penn, O. K. Farha, J. T. Hupp, D. G. Truhlar, C. J. Cramer and J. A. Lercher, *J. Am. Chem. Soc.*, 2019, **141**, 9292–9304.
37 H. Li, M. Eddaoudi, M. O'Keeffe and O. M. Yaghi, *Nature*, 1999, **402**, 276–279.
38 J. Lee, O. K. Farha, J. Roberts, K. A. Scheidt, S. T. Nguyen and J. T. Hupp, *Chem. Soc. Rev.*, 2009, **38**, 1450–1459.
39 S. M. Cohen, *Chem. Rev.*, 2012, **112**, 970–1000.
40 C. Kutzscher, G. Nickerl, I. Senkovska, V. Bon and S. Kaskel, *Chem. Mater.*, 2016, **28**, 2573–2580.
41 Y. Bai, Y. Dou, L.-H. Xie, W. Rutledge, J.-R. Li and H.-C. Zhou, *Chem. Soc. Rev.*, 2016, **45**, 2327–2367.
42 E. D. Metzger, R. J. Comito, C. H. Hendon and M. Dincă, *J. Am. Chem. Soc.*, 2017, **139**, 757–762.
43 H. Furukawa, K. E. Cordova, M. O'Keeffe and O. M. Yaghi, *Science*, 2013, **341**, 6149.
44 M. Kalaj and S. M. Cohen, *ACS Cent. Sci.*, 2020, **6**, 1046–1057.
45 K. Manna, T. Zhang, M. Carboni, C. W. Abney and W. Lin, *J. Am. Chem. Soc.*, 2014, **136**, 13182–13185.
46 R. Newar, R. Kalita, N. Akhtar, N. Antil, M. Chauhan and K. Manna, *Catal. Sci. Technol.*, 2022, **12**, 6795–6804.
47 T. Zhang, K. Manna and W. Lin, *J. Am. Chem. Soc.*, 2016, **138**, 3241–3249.
48 K. Manna, P. Ji, Z. Lin, F. X. Greene, A. Urban, N. C. Thacker and W. Lin, *Nat. Commun.*, 2016, **7**, 12610.
49 R. Newar, N. Akhtar, N. Antil, A. Kumar, S. Shukla, W. Begum and K. Manna, *Angew. Chem.*, 2021, **60**, 10964–10970.
50 N. Antil, A. Kumar, N. Akhtar, R. Newar, W. Begum, A. Dwivedi and K. Manna, *ACS Catal.*, 2021, **11**, 3943–3957.
51 X. Feng, P. Ji, Z. Li, T. Drake, P. Oliveres, E. Y. Chen, Y. Song, C. Wang and W. Lin, *ACS Catal.*, 2019, **9**, 3327–3337.
52 J. Shi, R. Han, S. Lu and Q. Liu, *J. Environ. Sci.*, 2021, **107**, 111–123.
53 J. A. Torres-Ochoa, D. Cabrera-German, O. Cortazar-Martinez, M. Bravo-Sanchez, G. Gomez-Sosa and A. Herrera-Gomez, *Appl. Surf. Sci.*, 2023, **622**, 156960.
54 I. Khalakhan, M. Vorokhta, X. Xie, L. Piliai and I. Matolínová, *J. Electron Spectrosc. Relat. Phenom.*, 2021, **246**, 147027.
55 A. Gaur, W. Klysubun, N. Nitin Nair, B. D. Shrivastava, J. Prasad and K. Srivastava, *J. Mol. Struct.*, 2016, **1118**, 212–218.
56 A. V. Kucherov, A. A. Slinkin, D. A. Kondrat'ev, T. N. Bondarenko, A. M. Rubinstein and K. M. Minachev, *Zeolites*, 1985, **5**, 320–324.
57 S. D. Tavernier and R. A. Schoonheydt, *Zeolites*, 1991, **11**, 155–163.
58 J. Dedecek, Z. Sobalik, Z. Tvaruazkova, D. Kaucky and B. Wichterlova, *J. Phys. Chem.*, 1995, **99**, 16327–16337.
59 A. Gaur and B. D. Shrivastava, *Rev. J. Chem.*, 2015, **5**, 361–39860.
60 A. R. Petersen, R. A. Taylor, I. Vicente-Hernandez, P. R. Mallender, H. Olley, A. J. P. White and G. J. P. Britovsek, *J. Am. Chem. Soc.*, 2014, **136**, 14089–14099.

61 V. M. Fernandez-Alvarez, S. K. Y. Ho and G. J. P. Britovsek, *Chem. Sci.*, 2018, **9**, 5039–5046.
62 S. Paria, Y. Morimoto, T. Ohta, S. Okabe, H. Sugimoto, T. Ogura and S. Itoh, *Eur. J. Inorg. Chem.*, 2018, **2018**, 1976–1983.
63 S. Paria, T. Ohta, Y. Morimoto, H. Sugimoto, T. Ogura and S. Itoh, *Z. Anorg. Allg. Chem.*, 2018, **644**, 780–789.